Nonlinear beam-dynamics calculations with an illustrative example

J. H. Whealton, B. D. Murphy, R. J. Raridon, K. E. Rothe, W. R. Becraft,* and T. L. Owens†
Oak Ridge National Laboratory, P.O. Box 2009, Oak Ridge, Tennessee 37831
(Received 26 July 1991)

Nonlinear beam-dynamics calculations are described that account for space-charge and image-charge effects. The calculation technique is explained and, as an illustration, is applied to two elements in an intense beam-combining funnel: an rf rebuncher and an rf deflector. For the case of the rebuncher, the calculations make use of the cylindrical symmetry of the device. For the deflector, both two-dimensional and three-dimensional calculations are performed. Emittance growth is analyzed for both the rebuncher and the deflector. For the rebuncher, a technique is proposed that considerably reduces the emittance growth.

PACS number(s): 41.80.−y, 29.17.+w, 41.70.+t

I. NONLINEAR BEAM-DYNAMICS CALCULATIONS

For a description of intense beam dynamics, nonlinear space-charge and image-charge forces must be included. The dynamic systems that we will consider for a nonlinear description including space charge and image charge are

$$\nabla^2\phi(\mathbf{r},t)=\int f(\mathbf{r},\mathbf{v},t)d\mathbf{v}\ , \tag{1}$$

$$\frac{\partial f(\mathbf{r},\mathbf{v},t)}{\partial t}+\mathbf{v}\cdot\nabla f(\mathbf{r},\mathbf{v},t)+\nabla\phi(\mathbf{r},t)\cdot\nabla_{\mathbf{v}}f(\mathbf{r},\mathbf{v},t)=0\ . \tag{2}$$

Equation (1) is the Poisson equation for an ion-distribution function, $f(\mathbf{r},\mathbf{v},t)$. Equation (2) is the Vlasov equation that describes the time evolution of this ion-distribution function.

The analysis technique can best be understood with reference to Fig. 1, which shows the path of the calculation. First, the Poisson equation is considered. For this first pass, the source terms are set equal to zero and a Laplace equation is solved by successive overrelaxation (SOR), finite difference, and boundary interpolation within a cell, using a Gauss-Seidel implicit method [1]. Iteration reduces memory requirements, and boundary interpolation contributes to the accuracy per cell. Generally, individual convergence of the solutions is not warranted on each pass, since the iteration procedure lends itself to incomplete convergence of the intermediate solutions. As noted before, the finite-difference method [2] compared with the finite-element method [3] has in our experience reduced memory requirements by a factor of 20 for a Poisson solution of the same accuracy. Boundary conditions for arbitrarily shaped metal surfaces can be specified as time-dependent Dirichlet conditions. Neumann boundary conditions can also be specified.

Second, the Vlasov equation is solved for a specified initial condition using the solution to the Laplace equation for a time step dt. The technique has been described [2,4] and significant advances in storage requirements and accuracy are reported. Some of this work [4] reports a speedup of the Vlasov solver by a factor of 10 from that reported elsewhere [5,6] while at the same time improving the accuracy by over a factor of 10. Resource utilization has been decreased [2] over results previously reported [3] by a factor of 400 with the same accuracy. The trivial relationship between the coordinates inside an element and the global elements for the uniform Cartesian grid used in this algorithm allows a factor-of-20 (of the 400) savings in the Vlasov solver over that obtained with irregular elements [3]. As mentioned [4] the Vlasov solver is made self-regulating in accuracy, and trajectory refinement is undertaken only in those places that need it.

Third, charge deposition is done in three dimensions by interpolation over the grid [2] and is "exact" in the sense that as the three-dimensional grid is made finer and the number of trajectories is increased, a result as accurate as desired can be obtained. Notice that nowhere is any paraxial-like assumption made, and the fields "to all orders" are directly calculated. Therefore, aberrations (to all orders) are also directly computed. Other nonlinear-optics effects computed include space charge to all orders caused by nonuniform beam density and/or boundaries. (Boundaries also cause nonlinear space-charge forces because they alter the dependence of Φ on r which is required for linearity.)

Fourth, the beam charge is taken as an inhomogeneous term to the Laplace equation solved in step 1 above. Now, one can also include an inhomogeneous plasma term which may be large, of opposite sign, extremely nonlinear, and three dimensional. This is the cause of numerical difficulties that were first surmounted in the two-dimensional steady-state case [5]. The technique used, accelerated under-relaxation, improved the prior art [7] by a factor of 1000 for the beam perveance of interest and by a greater factor for higher perveance. Another factor-of-10 increase in speed was achieved, while at the same time the accuracy was increased by more than a factor of 100 as reported [6]. This technique was extended to three dimensions [2,3]. Essentially the best technique we have found is to use an unconverged Newton SOR outside its established range of validity [8]. The inhomogeneous plasma term is not relevant to the calculations discussed here.

Fifth, the time is moved back by dt, the ions are moved

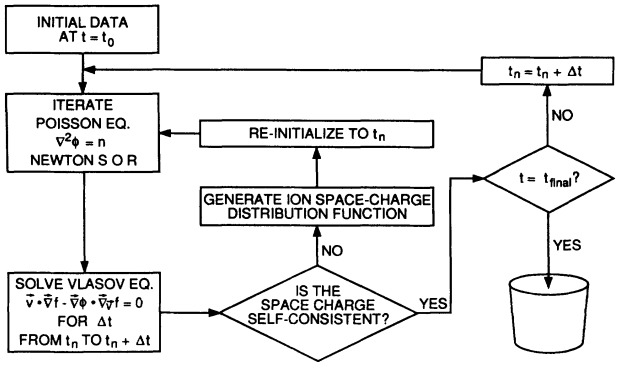

FIG. 1. Path of calculation for 3D time-dependent Vlasov-Poisson analysis.

back to their phase-space positions at that previous time, and the Vlasov equation is again solved with the new fields computed from the Poisson-equation solution of step 4. The trajectories are different from those computed in step 2 because of the presence of the space-charge terms (steps 3 and 4).

Sixth, since the trajectories of step 5 are different from those of step 2, steps 3, 4, and 5 are repeated (Vlasov-Poisson iteration) until no change obtains. This completes the convergence procedure and one can proceed to the next time step. However, one should note the implication of the iteration consisting of steps 5 and 6.

Seventh, the time is advanced by dt and steps 2 through 6 are repeated. Thus, the beam evolution through the device under consideration is followed.

II. ILLUSTRATION EXAMPLE: A FUNNEL

The concept of funnels was introduced in recent years with the idea of increasing beam intensity by combining two beams in the following fashion: The beam is, in each case, produced by an rf accelerator and thereby composed of bunches. The beam bunches are made to occupy relatively small fractions of the rf cycle in these cases. The respective bunches from the two beams, having been appropriately phased, are made to enter an rf deflector, which causes them to interlace. The funnel itself, in one embodiment called the magnetic funnel, is composed of many transport elements with strong transverse focusing produced by quadrupole permanent magnetic fields. An occasional rf rebuncher is introduced to recompress the bunches. Crucial elements of the funnel are the beam dynamics in the rf rebuncher and in the deflector. Beam dynamics in either case must be assessed using a detailed analysis of the kind we have described above.

Several components in a magnetic funnel [9] have been examined using a full three-dimensional (3D) solution to the time-dependent Vlasov-Poisson equations with all image charges included [10,11]. Specifically, the rms emittance growth of the subsystems is examined in detail. For the systems considered, a significant longitudinal emittance growth occurs. Details on the development of this emittance growth are studied. These systems were originally designed using the $2\frac{1}{2}$D-type analysis [12] which does not account for image charges and neglects azimuthal nonlinear space-charge forces. A highly resolved, accurate assessment of rms emittance growth has not been obtained with this original analysis. However, for the 3D analysis at least the precision is significant, as will be shown. First, we will consider the simple rebuncher; second, the rf deflector; and third, we will introduce a nonlinear longitudinal emittance-reducing "optical" element.

The rms longitudinal emittance growth is due to the longitudinal velocity kick being dependent on a transverse dimension as well as the longitudinal dimension forming an oblique surface in the three-dimensional phase space, z, V_z, and x. A plane surface parallel to z in this space has zero rms emittance. A curved surface or a plane not parallel to z in this space has finite rms emittance under the conventional definition:

$$\epsilon_{z,\mathrm{rms}}=\frac{\beta\gamma}{n}\left[\sum_j z_j^2\sum_j z_j'^2-\left[\sum_j z_j z_j'\right]^2\right]^{1/2}.$$

III. NONLINEAR BEAM DYNAMICS OF A FUNNEL: rf REBUNCHER

We turn now to an examination of a 425-MHz rebuncher on a 2-MeV beam. A typical rebuncher is illustrated in Fig. 2. It is cylindrically symmetric and these calculations will take advantage of that fact. An emittanceless beam bunch of constant density (water-bag distribution) is shown entering the fringe fields of an rf re-

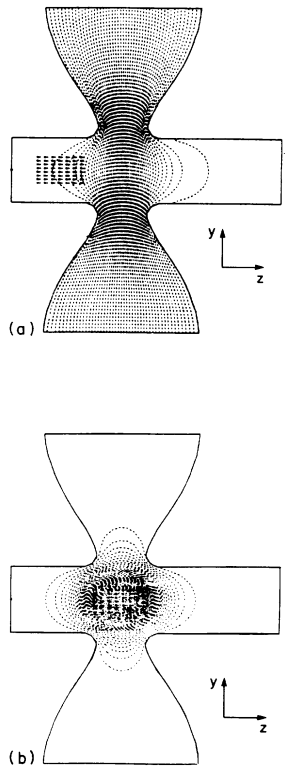

FIG. 2. Rebuncher at two different time periods: (a) when the rf field is at a maximum and (b) when the field is at a null.

buncher in Fig. 2(a). It should be kept in mind that when applying this technique to a particular experimental system, one would ideally have a matched beam. Our main purpose here, however, is to demonstrate the technique and we have thus chosen to use a cold beam. At the part of the cycle depicted in Fig. 2(a), the fields are near the maximum. When the center of the bunch is at the center of the rebuncher, the rf fields are at a null and only the space-charge and image-charge fields are present, as can be seen in Fig. 2(b). Longitudinal emittance as a function of time is shown in Fig. 3 for both zero and 100-mA beam current. The double-humped structure represents partial canceling of aberrational shear forces on both sides of the null field (denoted as $\Phi=0$ in Fig. 3). The partial cancellation occurs because of the extreme fringe fields such as those shown in Fig. 2(a). The radial center of the bunch is affected much more than the edges. As the bunch proceeds, the edge catches up, partially mitigating the aberrations. Immediately after the null, the edge is affected more than the center (overshoots) and the emittance climbs again. Near the trailing edge of the fringe fields, the center catches up again. The net result, at least in the case of zero beam current, is that most of the aberrations cancel (90%). The reason the rms emittance growth, at zero current, does not completely cancel is that some ion relative motion occurs during traversal of the rebuncher. However, in the high-current case in Fig. 3 there is a noticeable space-charge–image-charge component which is superimposed on the above-described shear aberrational phenomena.

The effect of bunch shape on longitudinal emittance is shown in Fig. 4 for a 100-mA beam (and for a somewhat different beam radius). The emittance growth for the hard (pillbox) beam (S0) is significantly greater than the softer (ellipsoidal) beams (S1 and S2); however, there is

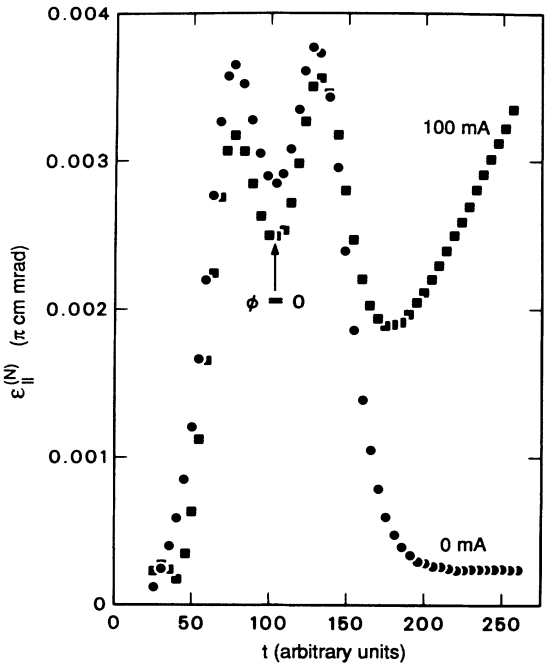

FIG. 3. Longitudinal emittance as a function of time (in arbitrary units) in an rf rebuncher.

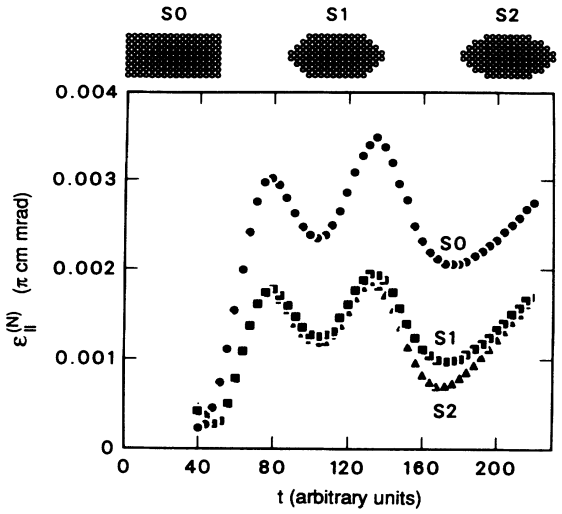

FIG. 4. Effect of bunch shape on longitudinal emittance in an rf rebuncher for a 100-mA beam.

not much difference between S1 and S2 over the region considered (numerical noise was found to be considerably lower than the emittance values of interest).

A longitudinal normalized rms emittance growth on the order of 0.003π cm mrad is expected for the "simple" rebuncher. Since there are several rebunchers, the total emittance growth due to rebunchers is expected to be higher than this. The complex double rebunchers, necessary near the rf deflector, will probably add more than this because of the possible degradation of mode purity; the smoothness of the phase-space distribution will possibly cause this to be halved. For the whole funnel, the total longitudinal emittance growth due to the rebunchers is probably greater than 0.005π cm mrad.

IV. NONLINEAR BEAM DYNAMICS OF A FUNNEL

A. rf deflector (2D)

Visualization of the behavior of an rf deflector is aided by reference to the three-dimensional isometric drawing shown in Fig. 5. Initially, we will discuss a two-

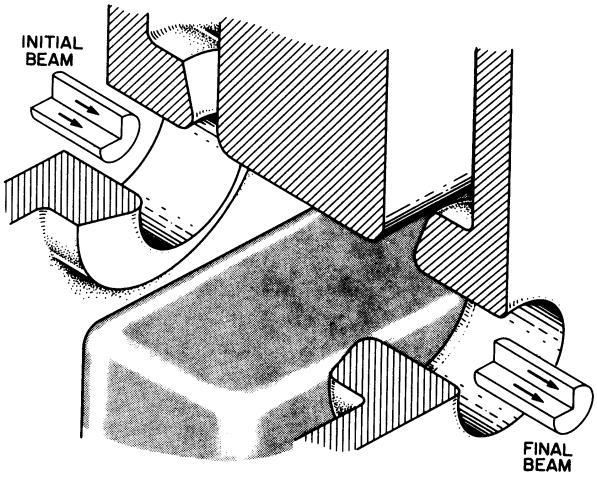

FIG. 5. Isometric drawing of an rf deflector.

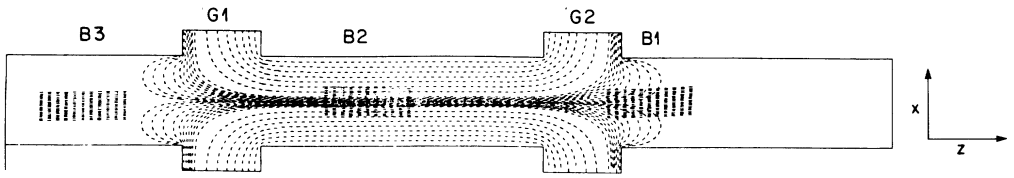

FIG. 6. An rf deflector with a zero-current beam in two-dimensional slot geometry, showing gaps G1 and G2 between the transport channel and the rf deflector and three beam bunches B1, B2, and B3 traversing the deflector, all moving to the right.

dimensional Cartesian variant of the deflector (Fig. 6). This is conventionally referred to as slot geometry. Figure 6 should be considered as a slice through the device. The situation is extended in the y direction. When making comparisons with 3D situations, we will simulate a given beam current by requiring the charge density in the slot geometry to be the same as for the particular beam in 3D. The errors introduced by the simplification of slot geometry will be discussed later. Three bunches in an rf deflector are shown at a particular instant of time in Fig. 6, labeled B1, B2, and B3. The dashed lines are electric potentials at that instant of time. For this figure, the beam space charge is zero. The potential contours are at linear increments: a coarse increment for extreme potentials and a finer increment near the center of the potential range where the beam bunch is located. Fringe fields due to the boundary conditions can be clearly seen in Fig. 6. The corresponding situation for a charge density equivalent to a 50-mA beam in three dimensions is shown in Fig. 7. Space-charge fields interact with the fringe fields in the case of bunch numbers 1 and 3 in Fig. 7, whereas the main steering field can be seen to be perturbed for bunch number 2.

Now we will consider the effect of a 425-MHz deflector on a beam composed of bunches occupying 28° of the rf cycle and which are 2.5 mm in height (see Fig. 8 and note that this is again slot geometry). The longitudinal emittance growth of such a beam is shown in Fig. 9 for both the 0-mA case and the 50-mA equivalent case. To get an idea of the properties of such a deflector, we consider first the time-reversed deflector. This is done for convenience. Time reversal does not introduce significant error into the calculations. Similar results apply either way when correctly interpreted. Slot geometry probably shows the emittance growth to within a factor of 2 in either the longitudinal or the transverse direction. Azimuthal nonlinear space-charge effects are neglected by such a representation. The main point of the computation is to get a clear idea of the space-charge, image-charge, and applied-field aberration issues as quickly as possible, so we can focus on the relevant causes.

In Fig. 8(a) a bunch is entering (leaving) the fringe fields of the deflector. The space-charge and image-charge fields are clearly interacting with the fringe fields. In Figs. 8(b) and 8(c) the time is near an rf null [as is Fig. 8(f)] and the space-charge fields dominate the applied rf fields. In Figs. 8(d)–8(e) the applied fields dominate, but are clearly perturbed by the space-charge fields.

The shear fields are partially canceled by having the field reversed in the gap. This is one of the advantages of having the field reversed in the gap. Another advantage is that these nonlinear shear fields will, on the average, be smaller in the gap since the rf fields are nearer zero. A major disadvantage is that the steering is mitigated as a result. As the bunch enters the first gap, the steering is initially in the wrong direction. When exiting the second gap, the steering is once again in the wrong direction. This results in the steering being less than intended. (In a test calculation, assuming no fringe fields, agreement was found to be within 0.1% when compared with a simple ballistic calculation.) Such a deficit in steering may appear at first sight to be an issue; however, to produce higher steering, say, 10% higher, requires higher fields in the deflection section which impact reliability and cause higher heat loading since the rf power to the device is proportional to E^2, so the rf power and heat loading must go up by about 20%. There may, in fact, be a heat-dissipation problem even without this inconvenience.

The effect of the deflector length on both steering angle and emittance growth is shown in Figs. 10 and 11, respectively. These calculations are for a 50-mA beam. A deflector length somewhat smaller than $\beta\lambda/2$ appears desirable since the steering increases a few percent with no reverse fringes to counter and the emittance growth is less (β is v/c and λ is the rf wavelength). In Fig. 10 one can clearly see that the steering is reduced because of field reversal in the gaps. Specifically, for a deflector length of $\beta\lambda/2$ the actual steering is 1.36° rather than 1.5° as planned.

Also shown in Fig. 11 is the situation without deflector

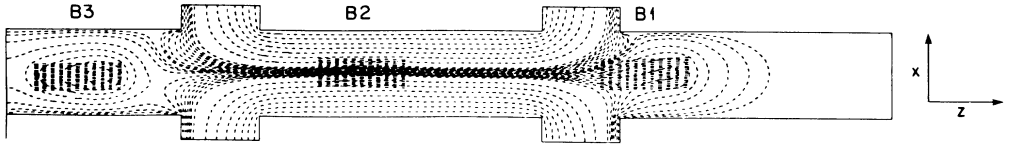

FIG. 7. An rf deflector in two dimensions with the equivalent of a 50-mA beam, showing three beam bunches B1, B2, and B3 traversing the deflector, all moving to the right.

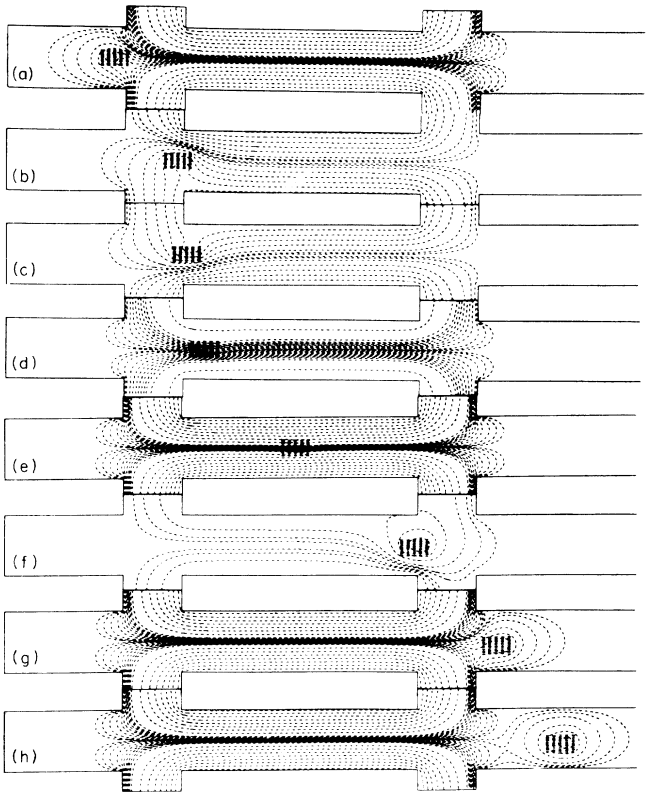

FIG. 8. Beam bunches occupying 28° of the rf cycle as they proceed through a 425-MHz rf deflector. These beam bunches are 2.5 mm in height (slot geometry).

fields (and therefore no field aberrations). The longitudinal emittance grows, even in this case, about the same as for the thin plate $T_D \approx 0.7\,\beta\lambda/2$ case, indicating that virtually all of this emittance growth is due to nonlinear space charge and image charge.

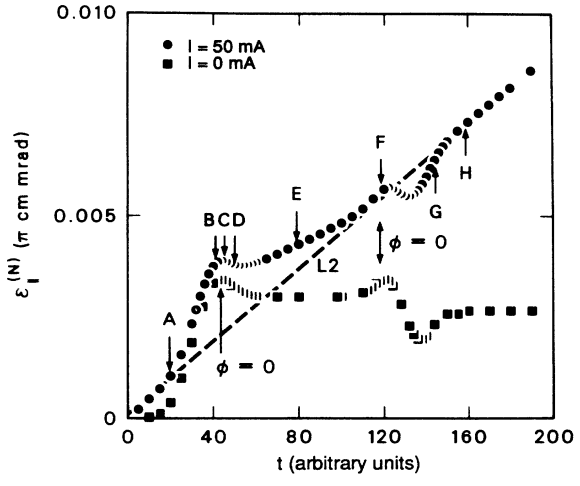

FIG. 9. Longitudinal emittance growth in the deflector shown in Fig. 8. Both the 0-mA and 50-mA cases are shown. The points *A* through *H* correspond to the configurations (a) through (h), respectively, as depicted in Fig. 8.

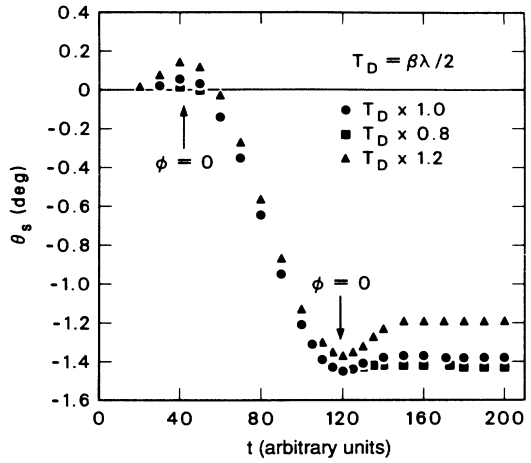

FIG. 10. rf deflector steering showing mitigation by fringe fields. Results for three different deflector lengths are shown. Deflector lengths are given in terms of the "cell length" $\beta\lambda/2$ ($\beta = v/c$ and λ is the rf wavelength).

Results for a 100-mA equivalent beam whose height is 4mm and longitudinal phase occupation is 28.30° are shown in Fig. 12 (together with the situation for the zero-current beam). This is qualitatively similar to Fig. 9. An important feature of both Fig. 9 and Fig. 12 is a qualitative difference between the emittance growth in the high-current case and the low-current case. The low-current case, when not affected by fringe fields, shows no rms emittance growth. However, the high-current case seems to suggest a prevailing emittance growth with time, or distance traversed, on which the shear aberrational fields are only a perturbation. This prevailing emittance

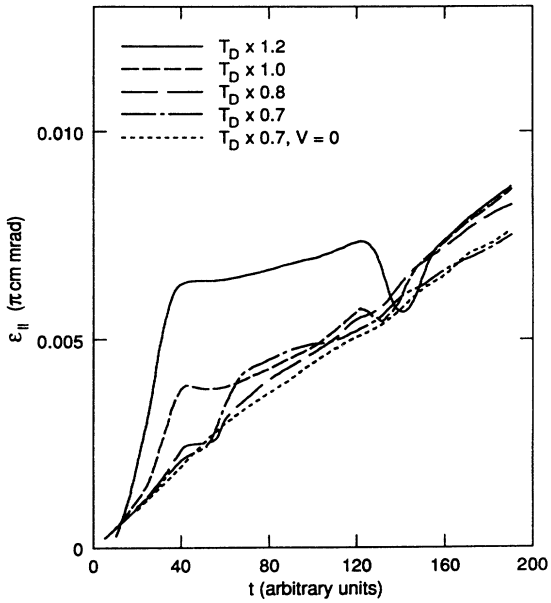

FIG. 11. Longitudinal emittance growth as a function of time for various length rf deflectors. The case without deflector fields is indicated by $V = 0$.

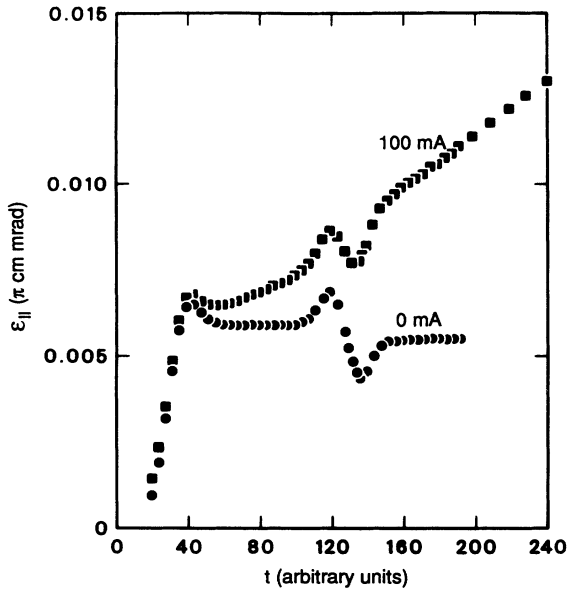

FIG. 12. Longitudinal emittance growth of a 100-mA beam (compared with a 0-mA beam) in an rf deflector as determined from a 2D calculation. It should be noted that this is qualitatively similar to the situation depicted in Fig. 9. However, the details of the two situations (pulse size and rf phase occupation) are not the same.

growth is caused by nonlinear space-charge forces and nonlinear image-charge forces and is denoted by the line L2 in Fig. 9.

B. Three-dimensional analysis of an rf deflector

The elements of the deflector in full 3D are shown in Fig. 13. For viewing purposes, the axes are not all to the same scale. The 2-MeV beam is chosen to be a square bunch and is seen drifting approximately in the middle of the device in Fig. 13. Because of the scale of the figure, the fact that the rf deflector plates are much longer than the space between them is not evident from the drawing. However, the spacing was indicated previously in the two-dimensional section; for example, Fig. 8 actually reflects the situation.

The longitudinal emittance growth for a three-dimensional deflector is shown as a function of time in Fig. 14. Here we see the characteristic emittance growth at the beginning for either 0-mA or 100-mA current. We see a gradual but slower emittance growth in the region of the rf deflector itself for the case of the 100-mA beam and no growth for the case of the zero-current beam. The various bunching effects due to the fringe fields are shown in both the 0-mA and the 100-mA cases and finally, the postdeflector variation is shown. There is no increase in emittance above a certain level for the zero-current beam, which is to be expected, but for the 100-mA beam there is again the characteristic nonlinear space-charge-induced longitudinal emittance growth. The results shown in Fig. 14 when compared with those in Fig. 12 (the equivalent 2D case) give an indication of the errors introduced by the simplification of slot

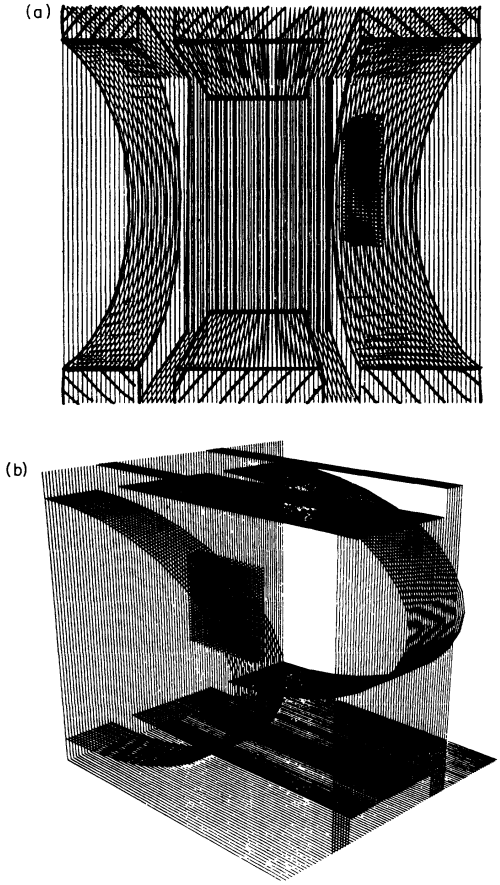

FIG. 13. A three-dimensional view of an rf deflector with a beam pulse. (a) is a side view showing the square pulse as it is about to exit the deflector; (b) is an oblique view showing half of the deflector and half of the pulse in the horizontal direction. This latter view has been expanded in the horizontal direction. Note that the scales are different in the different dimensions.

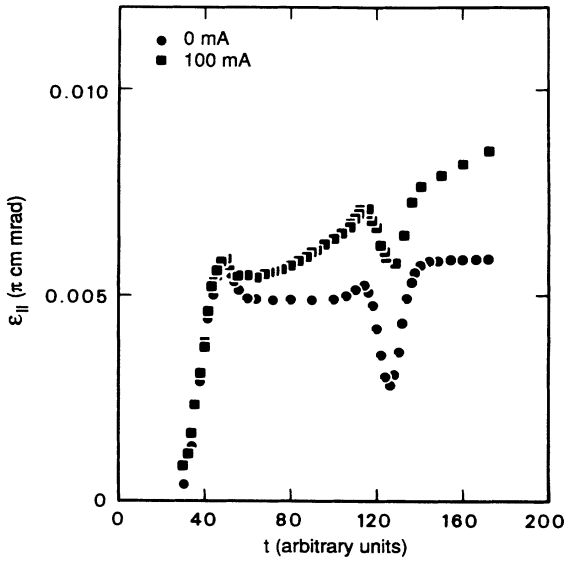

FIG. 14. Longitudinal emittance growth as a function of time (in arbitrary units) for an rf deflector as determined by a three-dimensional analysis. The 0-mA and 100-mA cases are shown.

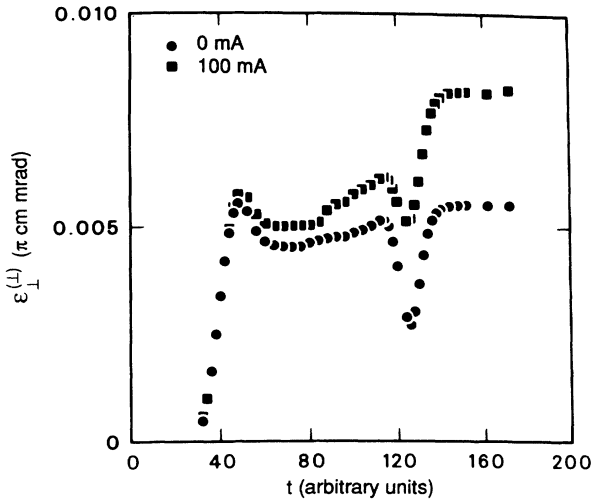

FIG. 15. Transverse emittance growth in an rf deflector determined by a three-dimensional analysis. This is the component which is transverse to the surfaces of the deflector electrodes. It is shown for both a zero-current and a 100-mA beam.

geometry. As the comparison shows, the 2D and 3D results are within 30% of one another. The emittance growth and the edge effects are seen to be lower in the 3D case and this is not unexpected since the aberrations in the 2D case are not mitigated by the electrodes in the third dimension.

In all of these cases, the initial distribution has zero emittance and all of the emittance that we see comes from the funnel itself. If the emittance were finite to begin with (e.g., for the case of a matched beam), then the emittance growth would presumably be less than is shown here. If the beam, for example, had an initial emittance of 0.005 and a current of 100 mA, then instead of the final emittance being 0.0085, as is shown here, it would probably be around 0.01, reflecting the emittance growth obtained when adding in quadrature with the initial emittance of the beam.

The component of the emittance transverse to both the beam direction and the surface of the deflector electrodes is shown in Fig. 15 as a function of time. Again, there are the usual edge effects as the beam bunch passes both ends of the deflection plate. Furthermore, in both the zero-current and 100-mA cases a significant emittance growth occurs because of noncancellation of these fringe-field effects from one end to the other.

In the case of a 100-mA beam, the emittance-growth calculations after traversal of the rf deflector give approximately 0.008π cm mrad for the longitudinal direction and for the transverse direction shown and slightly less for the other transverse direction.

V. NEW LONGITUDINAL rms EMITTANCE-REDUCING LENS

For a typical rebuncher, the longitudinal emittance growth for a hard (pillbox) beam bunch, as a function of distance traveled by the bunch, is shown by the curves in

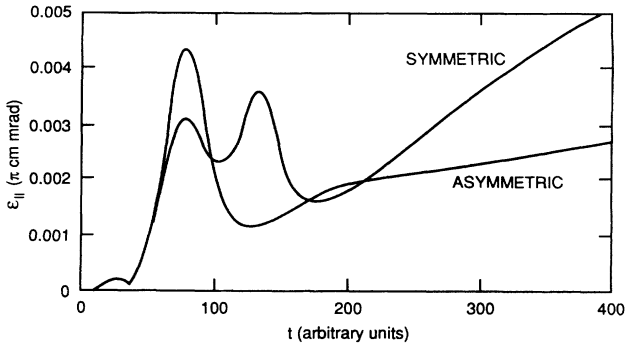

FIG. 16. Longitudinal emittance growth in a rebuncher for pillbox-shaped beam bunches. The curve labeled "symmetric" refers to the situation where the zero of the rf field occurs when the beam is at the center of the device. The curve labeled "asymmetric" refers to a situation where the zero of the field is offset such that it does not coincide with the bunch being at the center.

Fig. 16. The curve labeled "symmetric" refers to the conventional arrangement for a rebuncher, i.e., the zero of the field occurs when the bunch is at the center of the device. By adjusting the phasing of the bunch with respect to the rebuncher, it is possible to counteract some of the nonlinear space-charge–image-charge forces [11]. The successful use of this technique is indicated by the curve labeled "asymmetric" in Fig. 16 showing noticeable improvements in longitudinal emittance growth (approximately a factor of 2). The same effect was demonstrated using a soft (ellipsoidal) beam. Further development of this, and similar, techniques holds out the prospect of significantly enhancing beam quality.

Now consider Fig. 17, which refers to the symmetric case. It is similar to Fig. 16 but is continued for about twice the time and distance. It shows that the longitudi-

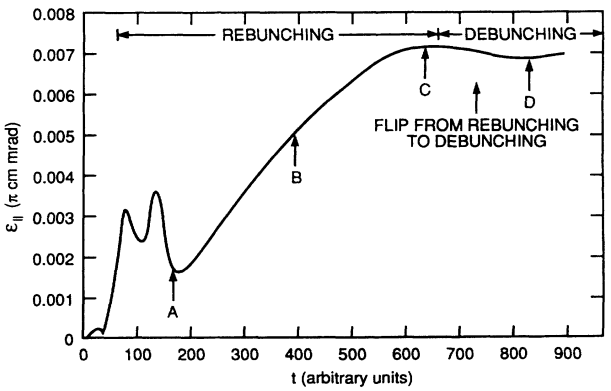

FIG. 17. The longitudinal emittance for pillbox-shaped beam pulses for the symmetric case shown in Fig. 16 and extended for a longer distance and time. Point *A* is towards the end of the rebuncher, *B* is typical of the drift space where the longitudinal emittance is increasing, *C* is where the emittance levels off, and *D* is where the emittance has dropped off and started to increase again. Parts *A* – *D* are all in a transport channel, as is shown in Fig. 18.

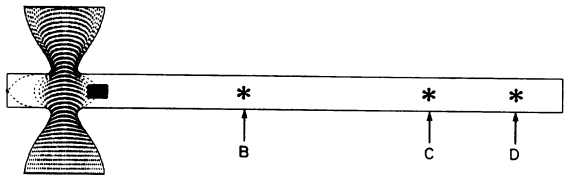

FIG. 18. An rf reburcher followed by a drift channel. The beam pulse is shown at point A of Fig. 17. Also shown are the positions corresponding to points B, C, and D of Fig. 17.

nal emittance of a bunch, as a function of time, increases after the region of the rebuncher, starting at the point labeled A. The longitudinal emittance continues to increase rather strongly in the drift space to beyond point B, until it levels off to a maximum at point C. It then dips about 10% and increases again. An examination of the beam in these four regions will show why the emittance has this property. Figure 18 is a simple rebuncher with a beam pulse. The location of this beam pulse corresponds to point A of the curve in Fig. 17. The rebuncher is joined by a transport channel with no fields but with a Dirichlet metal boundary condition. The beam simply drifts along this channel and the emittance is examined. In Fig. 18, as explained, the beam pulse is at point A. Also indicated in Fig. 18 are the positions corresponding to points B, C, and D of Fig. 17. Figure 19 shows the longitudinal emittance at points A, B, C, and D. Figure 19(a) is the longitudinal emittance at point A with the axial velocity as the vertical axis and the longitudinal position of the beam as the horizontal axis. The points fall approximately along a straight line indicating relatively low emittance. Slight aberrations occur at the ends. The velocity is characteristic of a rebuncher which means the beam is being compressed. Part (b) of Fig. 19 corresponds to point B in Figs. 17 and 18. The longitudinal emittance has obviously increased. The effect of significant aberrations, basically from nonlinear space-charge forces between A and B, can be seen in the longitudinal emittance diagram. This is consistent with Fig. 17. At point C, the longitudinal emittance [Fig. 19(c)] is seen to be very high and very different from point B. Essentially, the beam is crossing over from a bunched to a debunched case. At point D we can see that the beam is clearly debunching. Space-charge forces have caused the beam to expand. The beam continues to expand in a very nonlinear fashion. This kind of growth is a significant concern for intense unneutralized beams drifting in long transport systems where there is a requirement for a very low longitudinal emittance growth.

FIG. 19. Longitudinal emittance of a beam bunch in a drift channel following a rebuncher. Parts (a)–(d) of this figure correspond to points A–D in Figs. 17 and 18.

VI. SUMMARY AND CONCLUSIONS

A new nonlinear 3D beam-dynamics calculation is described and applied to a funnel. Emittance growth for two crucial elements in a funnel, a rebuncher and a deflector, has been calculated. The rebuncher calculations make use of the cylindrical symmetry of the device. In the case of the deflector, a simpler 2D calculation using slot geometry is found to give results within 30% of the complete 3D calculation. The calculations show what the optimum deflector length should be and that in such a case the nonlinear beam space charge and image charge dominates the longitudinal emittance.

A modification to the rebuncher is introduced and it is shown to reduce the longitudinal emittance growth by a considerable amount. In a drift channel following a rebuncher the calculations show how the longitudinal emittance grows.

Using full space-charge and image-charge calculations in both 2D and 3D we have shown that a typical funnel will probably contribute to a longitudinal emittance growth, end to end, of about 0.015π cm mrad, assuming perfect alignment according to calculations performed thus far. The transverse emittance growth is expected to

be slightly less, but still on the order of 0.010π cm mrad. By employing the modified rebuncher, the value for the longitudinal emittance may be decreased significantly. These conclusions may be important for applications involving rebunchers and funneling where beam emittance is of concern.

ACKNOWLEDGMENT

Our research was sponsored by the Office of Fusion Energy, U.S. Department of Energy, under Contract No. DE-AC05-84OR21400 with Martin Marietta Energy Systems, Inc.

*Also at, Grumman Space Systems, P.O. Box 3056, Oak Ridge, TN 37831.

†Present address: Fermi National Accelerator Lab., Accelerator Div., P.O. Box 500, Batavia, IL 60510.

[1] G. D. Smith, *Numerical Solution of Partial Difference Equations: Finite Difference Methods,* 2nd ed. (Oxford University Press, Oxford, 1978).

[2] J. H. Whealton, R. W. McGaffey, and P. S. Meszaros, J. Comput. Phys. **62**, 20 (1986).

Phys. **28**, 408 (1978); J. H. Whealton and J. C. Whitson, Part. Accel. **10**, 235 (1980).

[7] E. F. Jaeger and J. C. Whitson, Oak Ridge National Labratory Report No. ORNL/TM-4990, 1975 (unpublished).

[8] J. M. Ortega and W. D. Rheinboldt, *Iterative Solution of Nonlinear Equations in Several Variables* (Academic, New York, 1970).

[9] K. Bongardt *et al.* (unpublished); F. W. Guy, in *High-Current, High-Brightness and High-Duty Factor Ion Injec-*

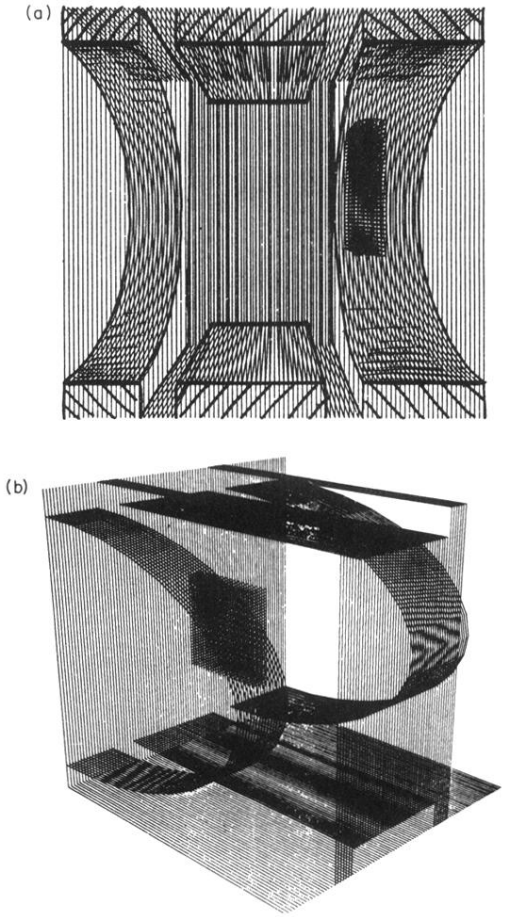

FIG. 13. A three-dimensional view of an rf deflector with a beam pulse. (a) is a side view showing the square pulse as it is about to exit the deflector; (b) is an oblique view showing half of the deflector and half of the pulse in the horizontal direction. This latter view has been expanded in the horizontal direction. Note that the scales are different in the different dimensions.

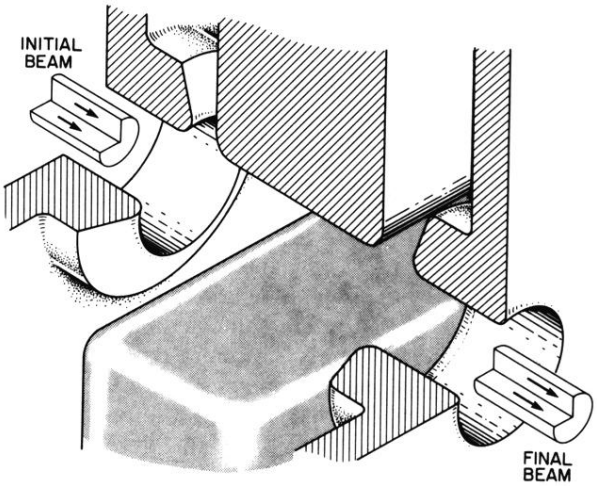

FIG. 5. Isometric drawing of an rf deflector.